Proceedings of the 21st ICSMGE, Vienna, Austria, 14 – 19 June 2026. Pistrol, Adam & Schweiger (eds.)
Published by: ÖGG, Austrian Society for Geomechanics, Salzburg, Austria, ISBN 978-3-9503898-4-5
https://doi.org/10.53243/ICSMGE2026-1935

Numerical Modelling of the Deeply Embedded Ring Anchor under Combined Loading

Ragini Gogoi
Texas A&M University, USA, raginigogoi@tamu.edu

Anas Aldawwas
Qassim University, KSA

Charles Aubeny
Texas A&M University, USA

Alejandro Martinez
University of California Davis, USA

Don DeGroot, Sanjay Arwade
University of Massachusetts Amherst, USA

Ryan Beemer
Virginia Tech, USA

ABSTRACT: As the floating offshore wind industry seeks innovative foundation solutions to reduce costs and improve efficiency, the Deeply Embedded Ring Anchor (DERA) has emerged as a novel approach by supporting multiple mooring lines with a single anchor point while offering enhanced geotechnical performance. This introductory study investigates DERA's behavior under inclined loading conditions in drained sand through numerical modeling and experimental validation. A three-dimensional finite element model was developed in ABAQUS and calibrated against reduced scale centrifuge tests performed on Ottawa F-65 sand. The investigation primarily focused on studying the influence of load inclination angles and embedment depths on anchor capacity, and on the characterization of failure mechanisms through a series of parametric studies. Based on these analyses, a predictive model for estimating the anchor's ultimate capacity is presented, along with a numerical disturbance function to address the installation-related disturbances observed in reduced scale tests. The results presented demonstrate a strong correlation between numerical predictions and experimental data, validating the model's reliability. This research establishes a quantitative understanding of DERA's behavior under inclined loading in sand, contributing to advancements in offshore anchor design.

KEYWORDS: Ring Anchor, Combined Loading, Offshore Geotechnics.

1 INTRODUCTION

The Deeply Embedded Ring Anchor (DERA) (renamed from the Multiline Ring Anchor, MRA, to emphasize its applicability for single line mooring connections as well) (Aubeny, et al., 2019) is emerging as a promising solution to address the growing demands for efficient, cost-effective, and sustainable anchoring systems in the offshore renewable energy sector. Designed to support floating offshore wind turbines and other offshore structures, DERA provides an innovative alternative to conventional anchor systems through its enhanced engineering performance and financial viability. This paper focuses on evaluating its geotechnical performance in drained sand under monotonic inclined loading conditions, contributing to its transition from conceptual design to practical application.

The anchor features a hollow cylindrical geometry with a vertical axis, open at both ends, and allows the attachment of multiple padeye on its outer surface for mooring line connections. This novel design enables DERA to function as a shared anchor system, supporting multiple floating platforms, and the emerging concept of networked offshore wind farms (Diaz, et al., 2016). Its capability to achieve deep embedment without depth restrictions allows it to mobilize higher soil resistances and resist substantial vertical and horizontal loads. Preliminary studies under controlled conditions show the anchor system as an efficient solution for supporting floating wind farms due to its structural simplicity, reduced fabrication and installation costs, and adaptability to various soil types (Lee, et al., 2020).

Previous studies have demonstrated favorable performance of DERA in clay, particularly in terms of geotechnical efficiency and cost-effectiveness (Aubeny & Lee, 2021) (Lee, et al., 2020) (Lee & Aubeny, 2021). In sand, it has presented promising results under purely vertical and horizontal load conditions (Gogoi, 2024) (Aldawwas, 2022). This paper investigates the response of the anchor under combined loading conditions in drained sand (Figure 1). A three-dimensional numerical model was developed to simulate the loading conditions acting on the anchor. The test load was applied at a single padeye, representing the resultant of the loads from the multiple mooring lines, as was demonstrated to be an efficient alternative by Fontana (Fontana, et al., 2018). This load application point was positioned along the side of the anchor wall, and its depth relative to the anchor length was studied extensively and concluded as a fundamental parameter in determining the inclined capacity of the anchor. The study was undertaken as part of a broader collaborative effort to assess the anchor's geotechnical behavior, addressing key aspects such as vertical and inclined load responses. The findings are intended to support the anchor's adoption in offshore renewable energy systems, providing sustainable and cost-effective foundation solutions for floating offshore structures.

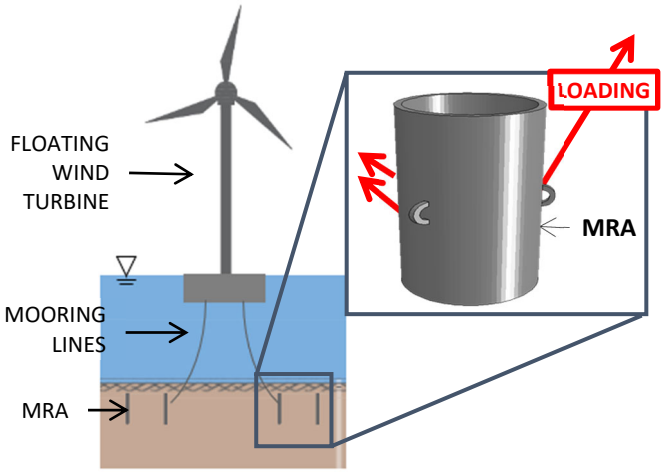

Figure 1. DERA subjected to inclined loading.

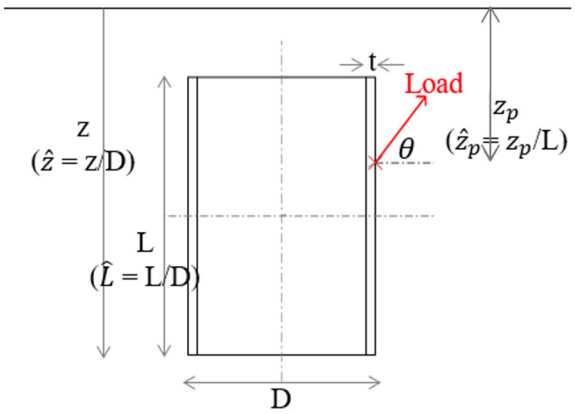

Figure 2. Geometry of DERA.

2 NUMERICAL MODEL

The numerical analysis in this study employed the finite element formulation in ABAQUS/Standard 6.12.1 to simulate the behavior of DERA under monotonic, inclined pullout in fully drained soil conditions. A fully coupled system was developed to perform transient analysis of a partially or fully drained porous medium, adopting the effective stress principle to describe soil behavior. Excess pore pressure generation was controlled in the model by limiting the load application rate to maintain a fully drained condition. A displacement-controlled loading was applied at a rate of ≤0.005 mm/s until failure, defined as 10% of the anchor diameter.

The FE model was conceptualized as a cylindrical soil mass with DERA at its center, embedded at a variable depth, to minimize complex mesh geometries (Figure 2, 3). The soil was modeled using 3D, 8-noded, coupled displacement and pore-pressure elements (C3D8RP) with first-order interpolation and reduced integration to mitigate shear locking and reduce computation time, with triangular prism elements (C3D6P) with full integration used at the central axis. The anchor was meshed with displacement elements (C3D8I) to reflect its negligible permeability and modelled as a rigid body, wished-in-place. Boundary constraints were applied to prevent movement at the base and outer edges of the model domain, sized at 2.5 times the embedment depth vertically and 3 times the anchor diameter radially. A geometric progression series was used to generate a graded mesh, with a higher degree of refinement near the anchor for accuracy while maintaining computational efficiency. The minimum element size was set at 0.1 m, and circumferential divisions at 40 to balance resolution and processing demands.

The soil-structure interactions were modeled using an isotropic Coulomb friction model along the walls of the anchor. At the tips, low-stiffness elastic elements of minimal element thickness addressed convergence errors and unrealistic stress concentrations by softening the soil response (Gogoi, 2024) (Gogoi, et al., 2021). These modifications were calibrated using parallel centrifuge tests, with reduction factors of 0.1 and 0.05 applied for the top and bottom tips, respectively.

Finally, the load application point, or padeye, was positioned along the side of the anchor, $(z_p; \hat{z}_p = z_p/D)$ as shown in Figure 2 and was adopted as a representative of the resultant force from the allowable multiple mooring lines. For an efficient application of the inclined loads in ABAQUS, a local coordinate system was defined for the padeye node by rotating its global coordinate system by a user defined angle, in this case – the load inclination angles, allowing inclined loads to be defined by a single axis numerically, thereby simplifying the analysis while preserving directional accuracy.

2.1 *Material parameters*

The study focused on medium dense – dense Ottawa F65 sand at a saturated unit weight of 20.18 kN/m^3. The elastoplastic Mohr Coulomb constitutive model with a non-associative flow rule was adopted to describe its behavior. A stress dependent Young's Modulus, E, defined in terms of the rigidity index was used to define the elastic response (Al Hakeem & Aubeny, 2019), with a Poisson's ratio, v, of 0.3, and a coefficient of earth pressure at rest dependent on the critical state friction angle $(1 - sin\,\varphi_{crit})$. The plastic response was defined using Bolton's equations for peak friction and dilation angles (with a triaxial configuration) as functions of the mean effective stress and soil relative density (Bolton, 1986), with a critical friction angle of 30° (Bastidas, 2016) (Vasko, 2015). For numerical convenience, a soil cohesion of 0.1 kPa was applied in the model as well. Additionally, the coupled response of the soil was defined using the built-in permeability model in ABAQUS/Standard based on Darcy's Law with the coefficient of permeability set equal to 0.00118 m/s at an initial void ratio of 0.5.

2.2 *Calibration of numerical model*

Reduced scale centrifuge tests conducted in parallel at the Center for Geotechnical Modeling at the University of

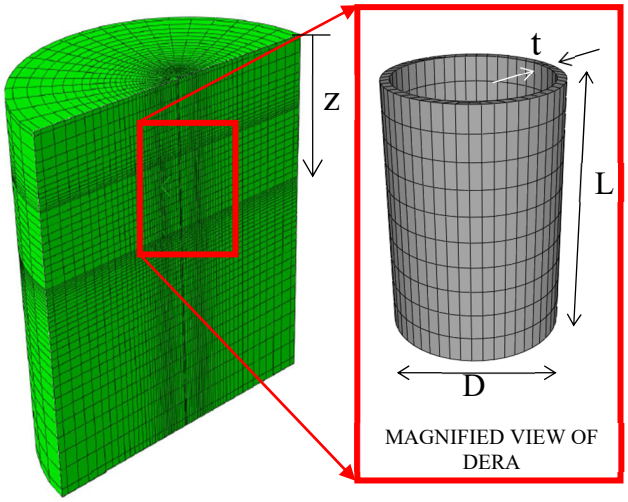

Figure 3. Cross-sectional cut 3D mesh of DERA.

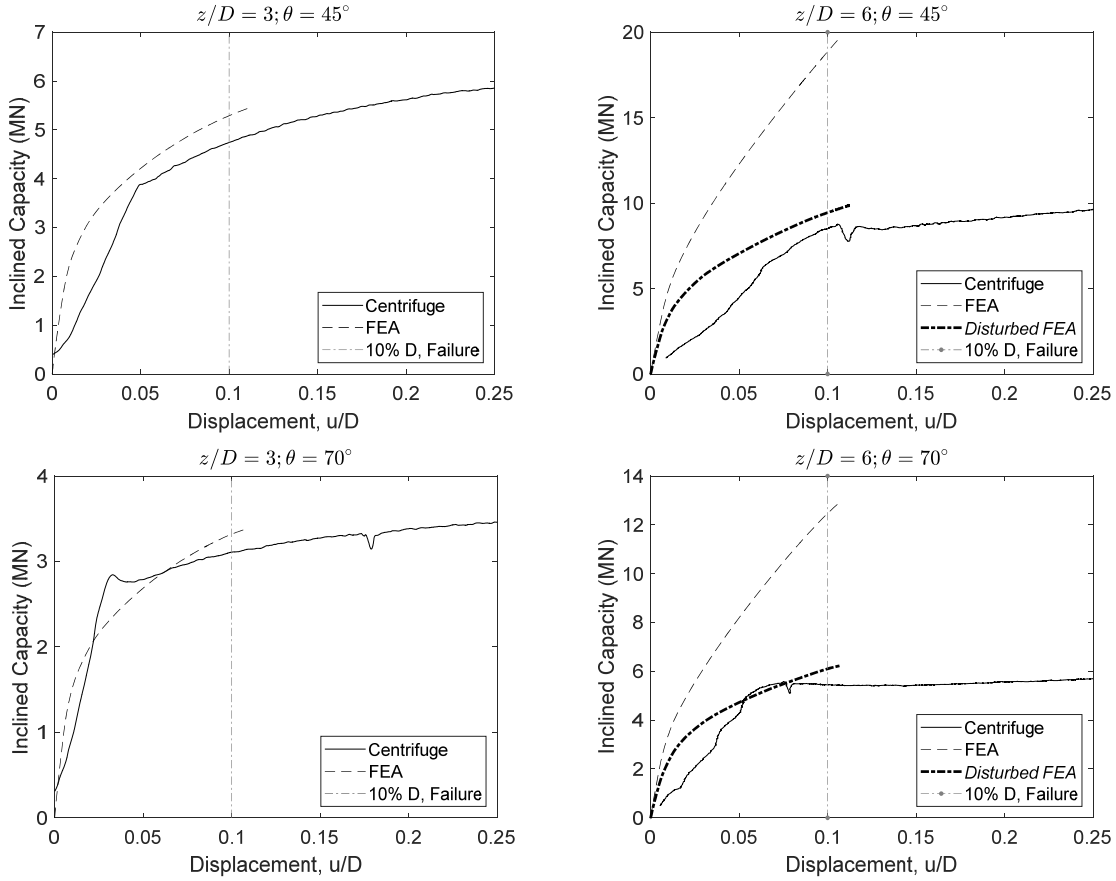

Figure 4. Load-displacement curves at shallow and deep embedment depths.

California Davis served as the calibrating tool for the numerical model described above (Huang, et al., 2024), for an anchor with dimensions (1g scale) of 2.8m (=D) diameter, 4.2m (=1.5D) length and 0.14m (=D/40) wall thickness. The physical tests were performed at 70g, using saturated Ottawa F65 sand with an initial density between 78.8% and 79.2%. For the test models, the load application points were strategically positioned at the intersection of the anchor's outer wall and a line extending 30° to the horizontal plane, and quasi-statically pushed to two embedment depths ($\hat{z} = z/D$) of three (shallow) and six (deep). The models were then subsequently loaded at inclination angles of 90°, 70°, 45°, and 30° to simulate taut mooring connections. The results of the physical tests with their corresponding numerical predictions are presented in the form of load-displacement plots in Figure 4. At the shallow embedment conditions, the predictions closely aligned with the measured data, with only minor deviations observed in the initial stiffness response at the lower angle. The predicted trend remained consistent with the overall measured data and capacities at failure were attained within acceptable limits.

Table 1. Predicted inclined capacities vs. Measured inclined capacity.

Load inclination angle [°]		**90**	**70**	**45**	**30**
SHALLOW EMBEDMENT, $\hat{z}$ = 3					
Centrifuge	Capacity [MN]	2.97	3.11	4.74	5.81
FEA	Capacity [MN]	3.01	3.38	5.46	7.49
	Difference [%]	1.41	8.73	15.16	28.91
FEA with *Dis$_f$*	Capacity [MN]	2.80	3.16	4.53	6.14
	Difference [%]	**5.81**	**1.78**	**4.40**	**5.65**
DEEP EMBEDMENT, $\hat{z}$ = 6					
Centrifuge	Capacity [MN]	5.21	5.45	8.51	6.72
FEA	Capacity [MN]	11.91 *5.57*	12.86 *6.24*	19.60 *9.89*	25.02
	Difference [%]	128.69 *6.95*	136.02 *14.52*	130.3 *16.21*	272.5
FEA with *Dis$_f$*	Capacity [MN]	5.53	5.36	8.41	6.68
	Difference [%]	**6.20**	**1.57**	**1.20**	**0.50**
(Disturbed finite element model predictions in italics)					

For the deeper embedment conditions, the discrepancies in the predictions and measured data were more pronounced. The FEA predictions exhibited higher initial stiffness, whereas the physical tests indicated softer responses with lower capacities. A similar discrepancy was noted in earlier studies of the project where the purely vertical load response of the anchor was studied (Gogoi, et al., 2023). The discrepancies observed were attributed to the installation disturbances encountered in the physical test, where the anchors were quasi-statically pushed in at 1g. This conclusion was supported by a reduction in the soil density within the soil column above the anchor measured during cone penetration tests performed post-spinning (Huang, et al., 2024). The initial soil density was reduced to 20%, indicating significant disturbances. The observed installation effects were incorporated into the numerical model by introducing a column of low-density soil above the anchor, while maintaining other characteristics of the original FEA model. The predictions of the disturbed FEA model are superimposed in Figure 4 and demonstrate significantly improved responses, closely following the measured trend. The observations reinforce the validity of the numerical models developed in the study to simulate the disturbed as well as undisturbed soil responses. However, due to the possibility of an oversimplified modeling of a complex real-world response, particularly soil densification caused by radial forces during installation, an empirical disturbance function, Dis_f (in SI units) is alternatively proposed, to be factored into the predictions of the original FEA model, to account for the observed installation effects. The disturbance function, Dis_f, was defined as a function of the load inclination angle and the soil stress level to represent more pronounced effects at higher anchor embedment depth.

$$Dis_f = \frac{yD_r}{\sigma'_v D^2} \quad (1)$$

$$y = -ax^2 + (36.1a + 45.7)x - 396.5a + 837.2 \quad (2)$$

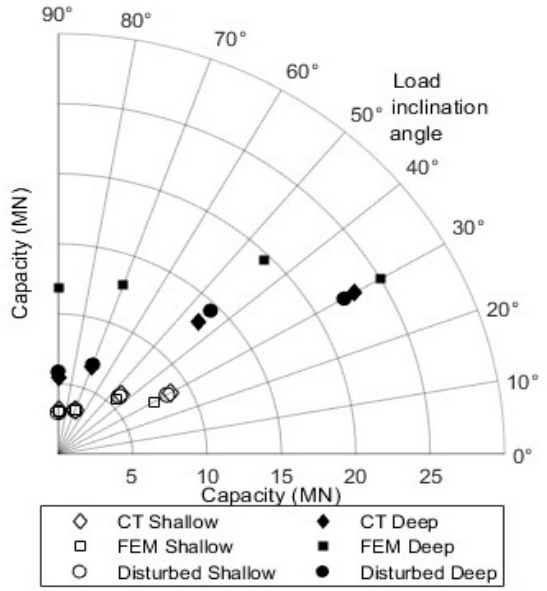

Figure 5. Inclined anchor capacities.

$$a = 0.041x^2;\ x = \frac{\sigma'_v \cos\theta}{D^2} \quad (3)$$

where θ is the load inclination angle (measured from the horizontal axis), σ'_v is the effective vertical soil stress at the bottom tip of the anchor, D is the anchor diameter and D_r is the initial soil density. The resulting capacities, defined at 10% of the anchor diameter for the current study, are summarized in Table 1, with their respective percentage differences from the measured data. Furthermore, the capacities are illustrated as *V-H* (vertical-horizontal) capacity interaction curves for both shallow and deep anchor embedment in Figure 5.

The behavioral response of the anchor is further depicted through displacement contours at failure, alongside the

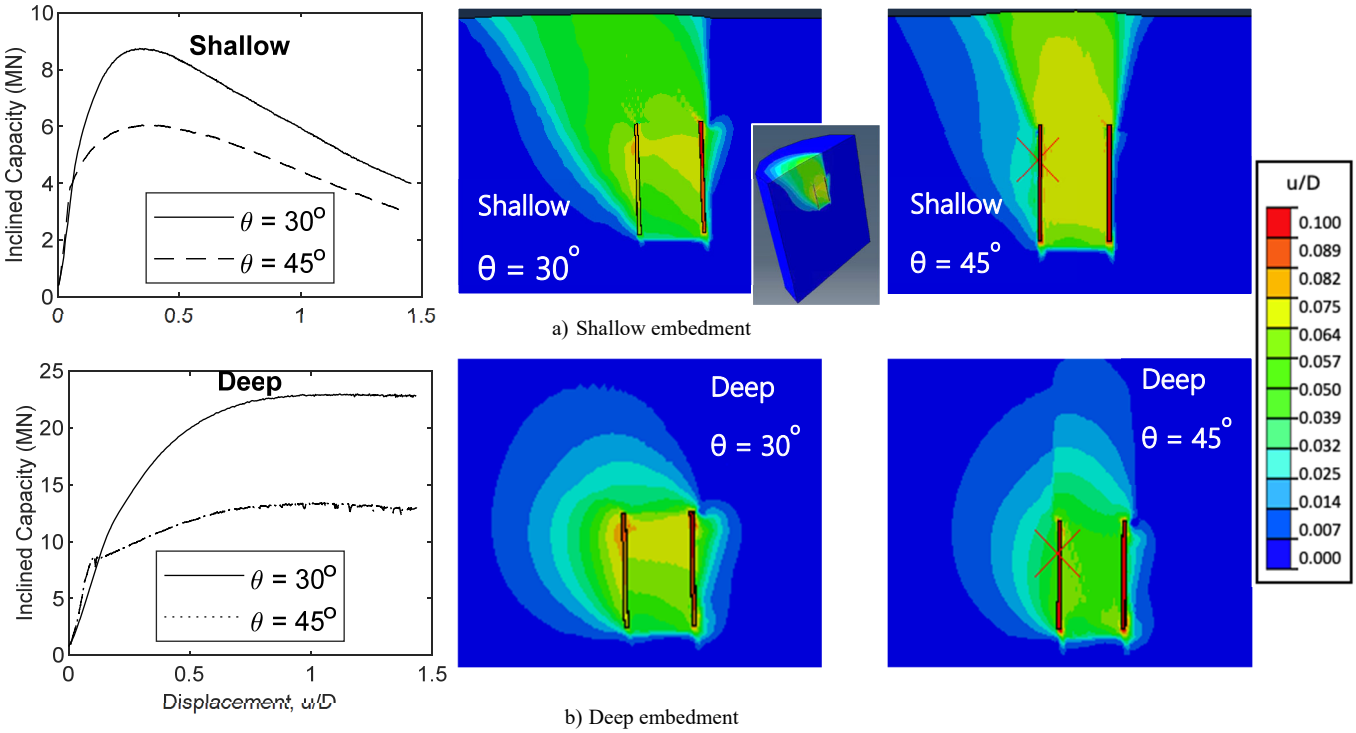

a) Shallow embedment

b) Deep embedment

Figure 6. Load-displacement curves from centrifuge (Huang, et al., 2024) and displacement contours (zoomed-in) from FEA at failure.

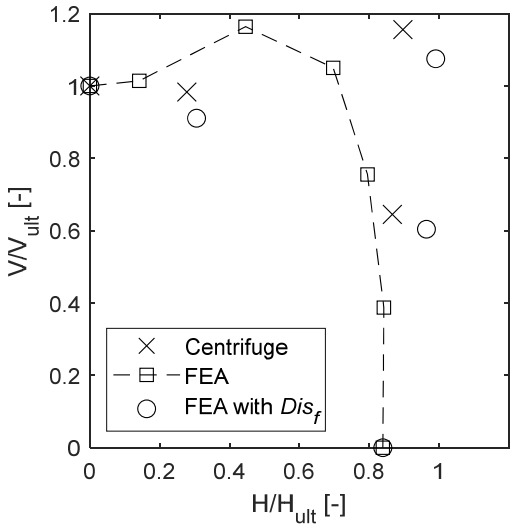

Figure 7. V-H capacity curve with disturbance function.

measured load-displacement curves to highlight the consistency observed in the failure mechanism. For the shallow embedment cases, the post-peak degradation observed in the measured load-displacement plots (Figure 6) suggested a surface failure mechanism, which was supported by the predicted wedge-shaped failure surfaces extending to the soil surface. In contrast, the absence of post-peak degradation in the deeper physical tests indicated localized failure mechanisms rather than surface failure, as corroborated by the numerical displacement contours. Additionally, the complete load-displacement data presents the large amount of reserved capacity available beyond the 10%D cutoff, mobilizing peak resistance only at larger displacements.

3 DETERMINATION OF INCLINED CAPACITY

Based on the calibrated numerical model, a calculation framework was developed to determine the ultimate capacity of DERA ($\hat{z} \geq 6$) under inclined load conditions. The framework generates estimations in the form of normalized *V-H* capacity curves, with the ultimate horizontal capacity, H_{ult} (Aldawwas, 2022) and the ultimate vertical capacity, V_{ult} (Gogoi, et al., 2025) as the normalizing factors (Figure 7). The ultimate vertical capacity has been previously described as a function of the anchor embedment depth, $\hat{z}$, and initial soil density, D_r. Developing the present framework in the selected normalized form significantly reduces computational demands by eliminating the influence of these parameters for the current analysis. The model was thus formulated as a function of the anchor aspect ratio, $\hat{L}$, and the padeye depth (load attachment depth), $\hat{z}_p$, with anchor diameter, *D* and wall thickness, *t*, kept constant at 2.8m and D/160, respectively. The current preliminary version was built on the predictions from a parametric study of different padeye depths, $\hat{z}_p$, and two anchor aspect ratios, $\hat{L}$, for the entire range of inclination angles to provide the following relationship:

$$\left(\frac{V}{V_{ult}}\right) = a\left(\frac{H}{H_{ult}}\right)^3 + b\left(\frac{H}{H_{ult}}\right)^2 + c\left(\frac{H}{H_{ult}}\right) + d \quad (4)$$

where V_{ult} and H_{ult} are the normalizing ultimate vertical and horizontal capacities, respectively; *V* and *H* are the vertical and horizontal components of the inclined capacity, Q_{inc}, such that,

$$V = Q_{inc} * \sin(\theta) \quad (5)$$

$$H = Q_{inc} * \cos(\theta) \quad (6)$$

with θ as the load inclination angle, and *a, b, c,* and *d* are quadratic functions of the normalized padeye depth, $\hat{z}_p$, defined as:

$$a = p_a \hat{z}_p{}^2 + q_a\, \hat{z}_p + r_a \quad (7)$$

$$b = p_b \hat{z}_p{}^2 + q_b\, \hat{z}_p + r_b \quad (8)$$

$$c = p_c \hat{z}_p{}^2 + q_c\, \hat{z}_p + r_c \quad (9)$$

$$d = p_d \hat{z}_p{}^2 + q_d\, \hat{z}_p + r_d \quad (10)$$

such that the coefficients are linear functions of the aspect ratio, $\hat{L}$:

$$p_a = 114.9\hat{L} - 71.2; q_a = -135.6\hat{L} + 86.2; r_a = 39.7\hat{L} - 31.9 \quad (11)$$

$$p_b = -175.2\hat{L} + 101.3; q_b = 202.3\hat{L} - 119.3; r_b = -60.2\hat{L} + 44.2 \quad (12)$$

$$p_c = 42.5\hat{L} - 23.9; q_c = -48.9\hat{L} + 26.5; r_c = 16.1\hat{L} - 11.5 \quad (13)$$

$$p_d = -2.1\hat{L} + 0.8;\ q_d = 2.5\hat{L} - 0.9; r_d = -0.6\hat{L} + 1.2 \quad (14)$$

Figure 8 presents the *V-H* capacity curves (solid lines) derived from the proposed framework, with the FEA predictions (discrete points) for different padeye depths, $\hat{z}_p$, for an anchor aspect ratio, $\hat{L}$, of 1.5. The calculated inclined capacity is finally factored with the proposed disturbance function, Dis_f, to account for potential installation effects:

$$Q_{inc_{dis}} = Q_{inc} * Dis_f \quad (15)$$

4 DISCUSSION AND CONCLUSION

The paper presents a numerical study on the performance of the deeply embedded ring anchor (DERA) in drained sand under combined loading conditions. Through the development of a calibrated 3D finite element model, the study investigates the anchor's response across different embedment depths and load inclination angles, providing critical insights into its capacity behavior and failure mechanisms.

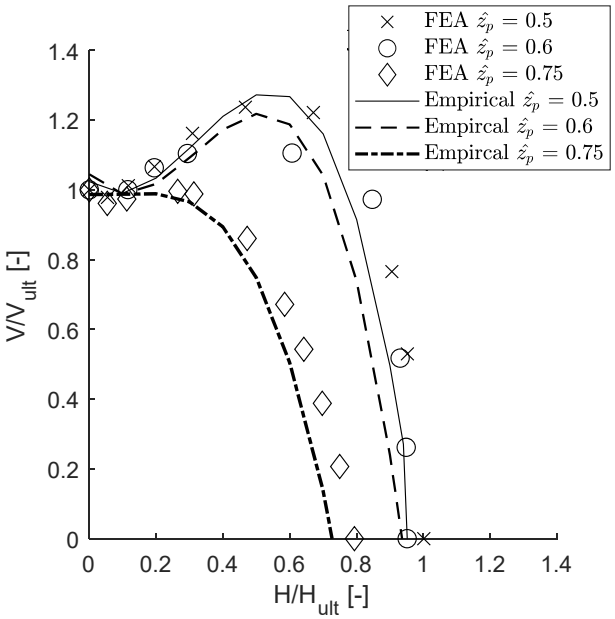

Figure 8. Evaluating predictions of the empirical model against FEA, for $\hat{L} = 1.5$.

The predictions from the finite element model closely followed the measured data for the shallow anchor embedment depths, whereas for the deeper embedment depths, a tentative increase in the influence of the installation effects observed in the physical tests led to significant discrepancies against the wished-in-place numerical predictions. Therefore, to account for the differences, a disturbance function was proposed, in an attempt to effectively bridge the gap between idealized numerical predictions and expected installation effects. The function was defined to account for the varying impact of the direction of loading and the anchor embedment depth on the expected installation disturbances based on observations during the physical testing.

Furthermore, a calculation framework was developed to estimate the inclined capacity of the anchor, presented in the form of normalized *V-H* capacity curves. The framework presents a practical tool to predict the anchor performance under selected anchor geometries and soil parameters while reducing computational demands but maintaining accuracy.

In conclusion, this study contributes to the advancement of DERA from conceptual design to practical application by refining predictive methodologies. The findings support its integration into offshore renewable energy systems, particularly in the development of shared anchoring solutions for networked floating wind farms. Future work may focus on extending the analysis to cyclic and long-term loading conditions, further validating the anchor's performance under operational offshore environments.

5 ACKNOWLEDGEMENTS

The authors would like to acknowledge the support from National Science Foundation, award number CMMI-1936901 and CMMI-1936939 and the Texas A&M High Performance Research Computing facility for the use of their resources in running the numerous finite element analyses supporting this study.

6 BIBLIOGRAPHY

Al Hakeem, N. & Aubeny, C. P., 2019. Numerical Investigation of Uplift Behavior of Circular Plate Anchors in Uniform Sand. *Journal of Geotechnical and Geoenvironmental Engineering.*

Aldawwas, A., 2022. *Ultimate Load Capacity of Caisson Foundations and Anchors in Sand.* s.l.:[Doctoral dissertation] Texas A&M University.

Aubeny, C. & Lee, J., 2021. *Horizontal load capacity of Multiline ring anchor in soft clay.* Austin, s.n.

Aubeny, C. P. et al., 2019. USA, Patent No. US 2020/0407021 A1.

Bastidas, A., 2016. *Ottawa F-65 Sand Characteristics.* Davis: [Doctoral Dissertation] University of California Davis.

Bolton, M., 1986. Strength and dilatancy of sands. *Geotechnique.*

Diaz, B. et al., 2016. *Multiline anchors for floating offshore wind towers.* s.l., IEEE.

Fontana, C. et al., 2018. Multiline anchor force dynamics in floating offshore wind turbines. *Winf Energy,* 21(11), pp. 1177-1190.

Gogoi, R., 2024. *A numerical study on the multiline ring anchor in sand.* s.l.:[Doctoral Dissertation] Texas A&M University.

Gogoi, R. et al., 2025. *Performance of Deeply Embedded Ring Anchor Under Vertical Loading in Drained Sand (under review).* s.l., s.n.

Gogoi, R. et al., 2023. *Numerical analyses of a multiline ring anchor for floating offshore wind turbines in sand.* London, ISSMGE.

Gogoi, R., Aubeny, C. & Watson, P. B. F., 2021. *Uplift Capacity of Suction Caissons in Sand for General Conditions of Drainage.* s.l., 40th International Conference on Ocean, Offshore and Arctic Engineering OMAE, ASME.

Huang, L. et al., 2024. Centrifuge modelling of the monotonic capacity of offshore ring anchors in sand.. *Deep Foundations Institute Journal,* p. 18(1).

Lee, J. & Aubeny, C., 2021. Lateral undrained capacity of a Multiline Ring Anchor in Clay. *International Journal of Geomechanics.*

Lee, J., Khan, M., Bello, L. & Aubeny, C., 2020. *Cost Analysis of Multiline Ring Anchor System for Offshore Wind Farm.* s.l., s.n., pp. 484-493.

Lee, J., Khan, M., Bello, L. & Aubeny, C., 2020. *Cost Analysis Of Multiline Ring Anchor Systems For Offshore Wind Farm.* Oxon Hill, s.n.

Vasko, A., 2015. *An Investigation into the Behavior of Ottawa Sand through Monotonic and Cyclic Shear test.* s.l.:[Master's Thesis] George Washington University .